

# Helical microtubules of graphitic carbon

Sumio Iijima

NEC Corporation, Fundamental Research Laboratories,  
34 Miyukigaoka, Tsukuba, Ibaraki 305, Japan

THE synthesis of molecular carbon structures in the form of  $C_{60}$  and other fullerenes<sup>1</sup> has stimulated intense interest in the structures accessible to graphitic carbon sheets. Here I report the preparation of a new type of finite carbon structure consisting of needle-like tubes. Produced using an arc-discharge evaporation method similar to that used for fullerene synthesis, the needles grow at the negative end of the electrode used for the arc discharge. Electron microscopy reveals that each needle comprises coaxial tubes of graphitic sheets, ranging in number from 2 up to about 50. On each tube the carbon-atom hexagons are arranged in a helical fashion about the needle axis. The helical pitch varies from needle to needle and from tube to tube within a single needle. It appears that this helical structure may aid the growth process. The formation of these needles, ranging from a few to a few tens of nanometres in diameter, suggests that engineering of carbon structures should be possible on scales considerably greater than those relevant to the fullerenes.

Solids of elemental carbon in the  $sp^2$  bonding state can form a variety of graphitic structures. Graphite filaments can be produced, for instance, when amorphous carbon filaments formed by thermal decomposition of hydrocarbon species are subsequently graphitized by heat treatment<sup>2,3</sup>. Graphite filaments can also grow directly from the vapour-phase deposition of carbon<sup>4,5</sup>, which also produces soot and other novel structures such as the  $C_{60}$  molecule<sup>6-8</sup>.

Graphitic carbon needles, ranging from 4 to 30 nm in diameter and up to 1  $\mu\text{m}$  in length, were grown on the negative end of the carbon electrode used in the d.c. arc-discharge evaporation of carbon in an argon-filled vessel (100 torr). The gas pressure was much lower than that reported for the production of thicker

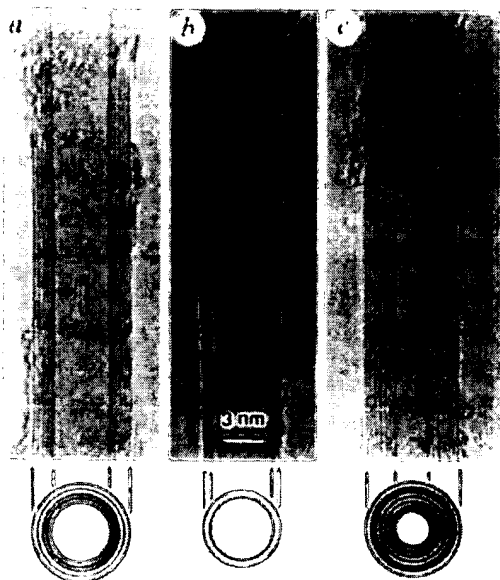


FIG. 1 Electron micrographs of microtubules of graphitic carbon. Parallel dark lines correspond to the {002} lattice images of graphite. A cross-section of each tubule is illustrated. *a*, Tube consisting of five graphitic sheets, diameter 6.7 nm. *b*, Two-sheet tube, diameter 5.5 nm. *c*, Seven-sheet tube, diameter 6.5 nm, which has the smallest hollow diameter (2.2 nm).

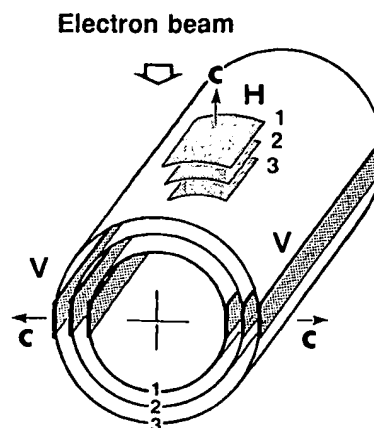


FIG. 2 Clinographic view of a possible structural model for a graphitic tubule. Each cylinder represents a coaxial closed layer of carbon hexagons. The meaning of the labels V and H is explained in the text.

graphite filaments<sup>5</sup>. The apparatus is very similar to that used for mass production of  $C_{60}$  (ref. 9). The needles seem to grow plentifully on only certain regions of the electrode. The electrode on which carbon was deposited also contained polyhedral particles with spherical shell structures, which were 5–20 nm in diameter. The needle structures were examined by transmission electron microscopy (electron energies of 200 keV).

High-resolution electron micrographs of typical needles show {002} lattice images of the graphite structure along the needle axes (Fig. 1). The appearance of the same number of lattice fringes from both sides of a needle suggests that it has a seamless and tubular structure. The thinnest needle, consisting of only two carbon-hexagon sheets (Fig. 1*b*), has an outer and inner tube, separated by a distance of 0.34 nm, which are 5.5 nm and 4.8 nm in diameter. The separation matches that in bulk graphite. Wall thicknesses of the tubules range from 2 to 50 sheets, but thicker tubules tend to be polygonized. This low dimensionality and cylindrical structure are extremely uncommon features in inorganic crystals, although cylindrical crystals such as serpentine<sup>10</sup> do exist naturally.

The smallest tube observed was 2.2 nm in diameter and was the innermost tube in one of the needles (Fig. 1*c*). The diameter corresponds roughly to a ring of 30 carbon hexagons; this small diameter imposes strain on the planar bonds of the hexagons and this causes two neighbouring hexagons on the ring to meet at an angle of  $\sim 6^\circ$ . For the  $C_{60}$  molecule, the bending angle is  $42^\circ$ , which is much larger than for these tubes. The C–C bond energy calculated for the  $C_{60}$  molecule is smaller than that of graphite<sup>11</sup>, suggesting that bending the hexagons in  $C_{60}$  lowers the bond energy. A similar effect of the bending on bonding energies might apply here. One of the key questions about the tubular structure is how the ABAB hexagonal stacking sequence found in graphite is relaxed, as it is impossible to retain this ideal graphite structure for coaxial tubes. There should be a shortage of 8–9 hexagons in going from one circumference of a tube to that inside it. Disordered graphitic stacking is known as turbostratic stacking, but no detailed accounts of stacking patterns in such structures have been reported. The argument here is also applicable to the spherical graphitic particles mentioned earlier<sup>6</sup>.

All the electron diffraction patterns (Fig. 3) taken from individual carbon needles are indexed by the  $\{h0l\}$  and  $\{hk0\}$  spots for hexagonal symmetry. The patterns always show strong (00*l*) spots when the needle axes are perpendicular to the [001] axis, supporting the idea of a coaxial arrangement of graphitic tubes. As shown in Fig. 2, two side portions of each tube (indicated by shading and labelled 'V') will be oriented so that the

(002) planes satisfy the Bragg diffraction condition for the incident electron beam, and thus give (00 $l$ )-type spots. Individual (002) planes in these portions are directly imaged in Fig. 1.

The  $\{hk0\}$  patterns as a whole show  $mm2$  mirror symmetry about the needle axis, and consist of multiple sets of  $\{hk0\}$  spots. For example, three sets of  $\{hk0\}$  spots seem to form ring patterns, only (100)- and (220)-type spots being seen (Fig. 3a). The diffraction pattern was obtained from a single tube consisting of seven sheets, confirmed by examining the electron microscope image. Referring again to Fig. 2, the top portion of the outermost tube, labelled 'H', and its counterpart on the bottom of the tube, give independently one set each of  $\{hk0\}$  patterns. If these two portions of the cylinder have the same orientation, they produce an identical  $\{hk0\}$  pattern. If three hexagon sheets on the tubes 1, 2 and 3 were oriented differently, they would give six different  $\{hk0\}$  spot patterns. Such a top-bottom effect is one of the requirements for the mirror symmetry. Another requirement is a helical arrangement of carbon hexagons on individual tubes, described further below.

Consider rotation of individual graphite sheets with respect to the needle axes. To explain the graphitic tube structure, the tube is cut at one side along the needle axis and unrolled. This is illustrated schematically in Fig. 4a. Fewer hexagons are drawn, than would form a real tube, but the essential needle geometry correctly represents one of our experimental diffraction patterns. A cylindrical tube can be formed by rolling up the hexagonal sheet about the filament axis (drawn by the heavy line) so as to superimpose hexagons labelled A and B at the top on A' and

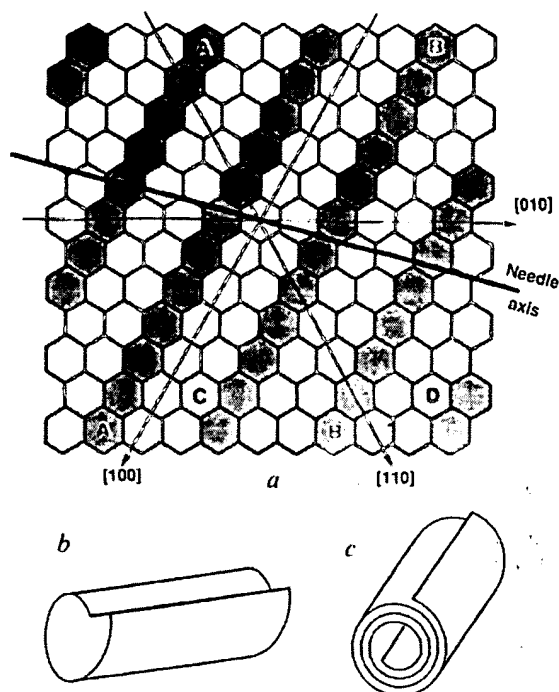


FIG. 4 a, Schematic diagram showing a helical arrangement of a graphitic carbon tubule, which is unrolled for the purposes of explanation. The tube axis is indicated by the heavy line and the hexagons labelled A and B, and A' and B', are superimposed to form the tube (for the significance of C and D, see text). b, The row of hatched hexagons forms a helix on the tube. The number of hexagons does not represent a real tube size, but the orientation is correct. c, A model of a scroll-type filament.

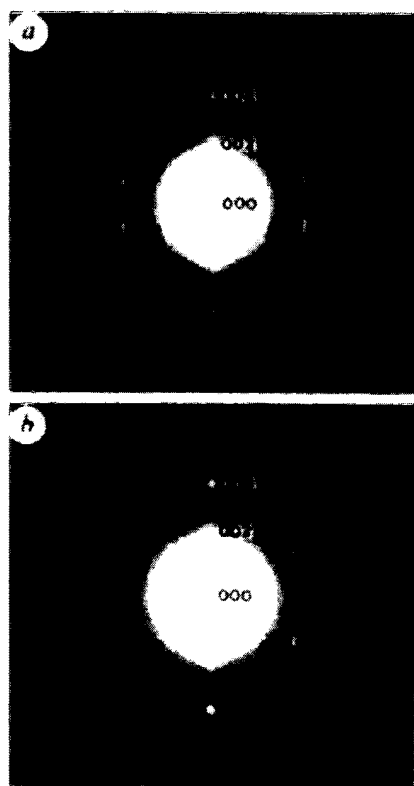


FIG. 3 Electron diffraction patterns from individual microtubules of graphitic carbon. The patterns show  $mm2$  symmetry, and are indexed by multiple superpositions of  $\{h0l\}$ -type reflections and  $\{hk0\}$  reflections of graphite crystal. The needle axes are horizontal. a, Superposition of three sets of  $\{hk0\}$  spots taken from a seven-sheet tubule. b, Superposition of four sets of  $\{hk0\}$  spots from a nine-sheet tubule.

B' at the bottom. It will be found that the hatched hexagons are aligned perfectly to make a helix around the needle axis (see Fig. 4b). The helical arrangement of the hexagons is responsible for the mirror symmetry as observed in the experimental diffraction patterns. One complete spiral rotation leaves a pitch three hexagons in height at the tip of the needle. There are many possible pitches in the helix, depending on the orientation of the sheet with respect to the needle axis. In other words, the orientation of a hexagon sheet can be determined uniquely by referring to the needle axis. If hexagons A and B coincide with those labelled C and D, the needle axis will be along [010] and thus there will be no spiral rows of hexagons. This has, however, rarely been observed.

Because of the helical structure, the  $\{hk0\}$  spot patterns should always contain sets of even numbers of spots. Occasionally, sets of odd numbers of spots occur, such as the groups of three shown in Fig. 3a. These can be explained by frequent coincidence of the top and bottom sheet orientations. Such an accidental coincidence will be increased for hexagonal symmetry of individual hexagon sheet when it is rolled. Consider the sets of four of  $\{hk0\}$  in Fig. 3b. Each of the sets of spots, which have equal intensity distributions, is rotated by  $\sim 6^\circ$  about the (000) origin, or the needle axis. We take one set of  $\{hk0\}$  spots (indicated by arrows), corresponding to one of the hexagon sheets, as a reference whose [100] axis is rotated by  $3^\circ$  about the needle axis. The other three sets of spots are then rotated by  $6^\circ$ ,  $12^\circ$  and  $24^\circ$  from the reference sheet. Considering the fact that the needle consists of only nine sheets and each set of  $\{hk0\}$  spots is generated from only three or four sheets, it is reasonable that every three or four sheets are rotated stepwise by  $6^\circ$  about the  $c$  axis. Any translational shift of the sheets cannot be detected in the electron diffraction patterns. A systematic change in sheet orientations was confirmed by  $\{h0l\}$ -type lattice image observations. The question of whether the systematic variation in the

rotation angles in successive tubules acts to stabilize the structure remains to be answered.

The tips of the needles are usually closed by caps that are curved, polygonal or cone-shaped. The last of these have specific opening angles of about 19° or 40°, which can be rationalized in terms of the way that a perfect, continuous hexagonal network can close on itself.

According to Bacon's scroll model for tubular needle growth, needles could be formed by rolling up single carbon-hexagon sheets to form tubular filaments as illustrated in Fig. 4c. Such filaments should have edge overlaps on their surfaces. But I have observed no overlapping edges for the needles described here. Instead, I have observed concentric atomic steps around the needles (I have not confirmed that these are helical). On the basis of these new experimental findings on needle morphologies, I propose a new growth model for the tubular needles. That is, individual tubes themselves can have spiral growth steps at the tube ends (Fig. 4b). It is worth mentioning that the spiral growth steps, which are determined by individual hexagon sheets, will have a handedness. The growth mechanism seems to follow a screw dislocation model analogous to that developed for conventional crystals, but the helical structure is entirely different from the screw dislocation in the sense that the present crystals have a cylindrical lattice. □

Received 27 August; accepted 21 October 1991.

1. Kroto, H. W., Heath, J. R., O'Brien, S. C., Curl, R. F. & Smalley, R. E. *Nature* **318**, 162–163 (1985).
2. Oberlin, A. & M. Endo *J. Cryst. Growth* **32**, 335–349 (1976).
3. Speck, J. S., Endo, M. & Dresselhaus, M. S. *J. Cryst. Growth* **94**, 834–848 (1989).
4. Tibbets, G. G. *J. Cryst. Growth* **68**, 632–638 (1984).
5. Bacon, R. *J. appl. Phys.* **31**, 283–290 (1960).
6. Iijima, S. *J. Cryst. Growth* **50**, 675–683 (1980).
7. Iijima, S. *J. phys. Chem.* **91**, 3466–3467 (1987).
8. Kroto, H. W. *Science* **242**, 1139–1145 (1988).
9. Krätschmer, W., Lamb, L. D., Fostiropoulos, K. & Huffman, D. R. *Nature* **347**, 354–358 (1990).
10. Whittaker, E. J. W. *Acta Cryst.* **21**, 461–466 (1966).
11. Saito, S. & Oshiyama, A. *Phys. Rev. Lett.* **66**, 2637–2640 (1991).

ACKNOWLEDGEMENTS. I thank Y. Ando for the carbon specimens.

## Evidence from Antarctic ice cores for recent increases in snow accumulation

V. I. Morgan\*, I. D. Goodwin\*, D. M. Etheridge† & C. W. Woakey\*

\* Australian Antarctic Division, Channel Highway, Kingston 7050, Australia

† CSIRO, Division of Atmospheric Research, Mordialloc, Victoria 3195, Australia

LARGE uncertainties exist in the present knowledge of the mass budget of the Antarctic ice sheet, because of a lack of data on the rates of both ice outflow and snow accumulation<sup>1</sup>. Present estimates indicate that both the outflow and the net accumulation are approximately equal to 2,000 km<sup>3</sup> of ice per year (equivalent to about 6 mm of sea level)<sup>2</sup>. The temporal variation of accumulation rate is central to determinations of the mass budget, because accumulation can change rapidly in response to short-term climate variations, whereas ice flow varies only on longer timescales. Here we present time series showing changes in the net rate of snow accumulation since 1806 along a 700-km segment of East Antarctica. The accumulation record was derived from the thicknesses of annual layers in ice cores, deduced from seasonal variations in oxygen isotope ratio and in ice-crust stratigraphy. We find a significant increase in the accumulation rate following a minimum around 1960, leading to recent rates that are about 20% above the long-term mean. If this recent increase is widespread, as suggested by shorter-term accumulation data from across a large

TABLE 1 Accumulation data for Wilkes Land sites

Site	Latitude	Longitude	Elevation (m)	Accumulation rate (kg m <sup>-2</sup> yr <sup>-1</sup> )	Accumulation change (%)	
				1975–85	1975–85 to 1955–65	1975–85 to 1930–85
DSS	66° 46' S	112° 59' E	1,370	570	37	19
DE08	66° 43' S	113° 12' E	1,200	1,160	43	28
GD03	69° 00' S	115° 30' E	1,828	355	23	15
GD15	69° 00' S	130° 48' E	2,155	356	26	21

part of Antarctica, the positive imbalance (5–25% of the mass input) shown in recent studies of the ice sheet's mass budget<sup>1</sup> may have existed only since the late 1960s. We estimate that this increase in accumulation rate should contribute to a lowering of sea level of 1.0–1.2 mm per year.

The records come from four ice cores drilled 100–300 km from the coast in Wilkes Land (Fig. 1). Sites DSS and DE08 are located close together (separation 18 km) near the summit of Law Dome in a high accumulation zone. The recent (1978–1987) mean accumulations for the DSS and DE08 sites are 570 and 1,160 kg m<sup>-2</sup> yr<sup>-1</sup>, respectively. The other two sites, GD03 and GD15, are located on the East Antarctic inland ice sheet in a moderate accumulation zone with recent (1978–1987) mean accumulations of 355 and 356 kg m<sup>-2</sup> yr<sup>-1</sup>, respectively<sup>3</sup>.

The thicknesses of the annual accumulation layers were determined by oxygen-isotope ( $\delta^{18}\text{O}$ ) and ice-crust stratigraphy on the cores. The coastal DSS and DE08 cores show exceptionally well preserved annual cycles of  $\delta^{18}\text{O}$  because the annual accumulation rates are high and surface melting rarely occurs. In addition, the mixing of surface snow is minimal as both sites are located near the summit of Law Dome where strong surface winds are infrequent (automatic weather station data; I. Allison, Australian Antarctic Division, personal communication). In parts of the cores where the  $\delta^{18}\text{O}$  data are ambiguous, electrical conductivity<sup>4</sup> and hydrogen peroxide<sup>5</sup> measurements, which also show annual cycles, were used for clarification. The inland GD03 and GD15 cores are located in a different snow accumulation regime where strong katabatic winds redistribute the precipitation<sup>6</sup>. Despite this mixing, there is an annual cycle in  $\delta^{18}\text{O}$ , although it is not as clear as in the Law Dome cores. The GD03 and GD15  $\delta^{18}\text{O}$  data were supplemented by visible stratigraphy techniques based on identification of an ice crust and wind slab layer which forms annually in autumn and overlies a summer depth hoar layer. For GD03 and GD15 (but not for DSS and DE08) this stratigraphic interpretation was confirmed by stake height measurements of recent accumulation and a reference horizon determined from gross  $\beta$ -radioactivity profiling.

We converted the thickness data from the cores into annual accumulation rate records by allowing for the densification of snow at depth, the upstream variation in snow accumulation (because the ice at depth originated upstream of the borehole) and the vertical strain due to ice flow<sup>7</sup>. Accurate corrections for the densification of firn in the upper layers were made from detailed density measurements on the cores. The correction for the upstream accumulation gradient is negligible for DSS, GD03 and GD15. For DE08 we used the present-day accumulation gradient to calculate a correction of +5% for the deepest ice, reducing linearly to zero at the top of the core. Thinning due to vertical strain in the ice is significant only in the longer DE08 and DSS records. Corrections were made by using measurements of the horizontal strain rate (either direct measurements of strain or calculated from surface velocities) around the boreholes. The calculated strain rates are close to those required to give ice sheet balance with the long-term mean accumulation rate. The vertical strain corrections for the bottom layers in the cores are +8.5% for DSS and +12% for DE08 and are reduced linearly to zero at the surface.